Journal of Thermal Engineering
https://jten.yildiz.edu.tr/
https://doi.org/10.47481/jten.0084

RESEARCH ARTICLE

Statistical analysis of magnetohydrodynamic Darcy–Forchheimer Sisko hybrid nanofluid flow over a bilinear stretching sheet with heat and mass transfer effects

K. Nirisha[1], V. Nagaradhika[2,*], Manjunatha S.[3]

[1]Department of Mathematics, GSS, GITAM Deemed to be University, 530045, Visakhapatnam, India
[2]Department of Mathematics, Sir M Visvesvaraya Institute of Technology, 562 157, Bengaluru, India
[3]Department of Mathematics, Sir M Visvesvaraya Institute of Technology, 562 157, Bengaluru, India

Abstract

In this work, as a model for manufacturing coating processes, the thermal and solutal magnetohydrodynamic (MHD) flow of a Sisko hybrid nanofluid (AA7072 and AA7075 nanoparticles dispersed in methanol) over a bilinear stretching sheet next to a porous medium is investigated. The model includes Forchheimer inertial drag effects, heat source, chemical reaction, and thermal radiation. The study also considers boundary conditions for convective heating. Using similarity transformations, a system of nonlinear ordinary differential equations is derived from the original nonlinear partial differential conservation equations. This system is solved with transformed boundary conditions using the MATLAB bvp4c solver, and the results are verified for consistency and reliability. Graphical representations are used to examine the effects of several control parameters, such as the Sisko fluid parameter, radiation parameter, magnetic field parameter, Forchheimer parameter, and Schmidt number, on the transport characteristics. Using response surface method (RSM), we calculated the Nusselt and Sherwood numbers and the skin-friction components on the stretching surface. The results are confirmed using specific cases from previously published studies. According to the results, an increase in the Sisko fluid parameter increases the velocity profile, while it decreases the temperature and concentration profiles. Furthermore, increasing the magnetic-field parameter increases the velocity boundary-layer thickness. R^2 value using Sherwood number and adjusted R^2 were equal to 100%. This study sheds light on the dynamics of nanofluids in MHD systems, which have significant consequences for energy generation, electronic cooling, processing of magnetic materials, and other areas of chemical and biomedical engineering that rely on enhanced heat transfer.

Keywords: Magnetohydrodynamics (MHD), Sisko fluid, AA7072–AA7075/methanol hybrid nanofluid, chemical reaction, slip boundary conditions, Darcy–Forchheimer porous medium, heat source, response surface method (RSM)

Cite this article as: Nirisha, K., Nagaradhika, V., & Manjunatha, S. (2026). Statistical analysis of magnetohydrodynamic Darcy–Forchheimer Sisko hybrid nanofluid flow over a bilinear stretching sheet with heat and mass transfer effects. Journal of Thermal Engineering, 12(6), 2069–2085. https://doi.org/10.47481/jten.0084

1. Introduction

The intricate rheology of fluids has prompted several researchers in the field of contemporary technology to investigate methods for analyzing these fluids. Because their properties differ markedly from those of Newtonian fluids, these fluids have extensive applications in engineering processes and industries. These fluids are known as non-Newtonian fluids because their relationship of stress to strain rate is nonlinear. Many commonplace items have fluids that do not behave like Newtonian fluids. These include foodstuffs, molten plastics, lubricants, paints, ketchup, emulsions, medications, toothpaste, grease, personal care items, biological fluids, mud, and many others. Investigating the thermophysical characteristics of these fluids is crucial because of their diverse nature and many applications in industry, mechanics, and biology. The properties of non-Newtonian fluids are described by the power-law fluid model; however, many other models have been proposed in the literature for studying these fluids. In regions with high shear rates, however, the power-law fluid model cannot be used to analyses fluid properties. Sisko introduced the Sisko fluid model in 1958 to address this constraint. The

*Corresponding Author
E-mail Adress: nagaradhika79@gmail.com

Submitted: 21 November 2025; **Accepted:** 12 March 2026

This paper was recommended for publication in revised form by Editor-in-Chief Ahmet Selim Dalkılıç

Published by Yıldız Technical University, İstanbul, Türkiye
This is an open access article under the CC BY-NC license (http://creativecommons.org/licenses/by-nc/4.0/).

Sisko model can be used to investigate pseudoplastic and dilatant properties of fluids. This is an extension of both the Newtonian and power-law fluid models that incorporate three parameters. Sisko studied suggested framework [1], over convective boundary conditions using lubricating grease. Torikul et al. [2], investigated the heat transmission process of a stretchy Sisko fluid while considering the impacts of porous media and a magnetic field. An increase in Sisko fluid has little impact on the velocity distribution. A thorough numerical analysis of the mass and heat transfer properties in Sisko nanofluid flow over a porous stretched sheet subjected to an inclined magnetic field was conducted by Manoj et al. [3]. The motion of mass and heat in non-Newtonian Sisko fluids when they travel over a bi-directionally stretched heated substrate in three dimensions, which include the MHD effect and heat radiation, is investigated by Sohail et al. [4]. The intriguing dynamics of a magneto-Sisko fluid in two dimensions were examined by Adilakshmi et al. [5] using heat production and nonlinearly stretchy sheet embedded in a porous medium as their models. Whenever the Sisko parameter is increased from 1.0 to 2.0, the velocity increases by 20%, while the temperature and concentration profiles decrease by 8% and 10%, respectively. Using an electromagnetically inclined sheet, Shakhil et al. [6] describes the convective flow of Sisko fluid. Fluid mobility is reported to have been improved due to the Sisko fluid properties and stronger electromagnetic fields. In their study, Bhanu et al. [7] viewed the three-dimensional steady state flow of MHD for a Sisko nanofluid. An increase in the magnetic parameter improves the temperature profile and reduces the velocity. The hybrid nanofluid, consisting of had aluminum alloy nanoparticles AA7072 and AA7075 within a methanol base fluid, was investigated by Abbas et al. [8]. Shanmugapriya et al. [9] investigated thermal energy transfer using nanoparticles of AA7072 and AA7072 + AA7075 alloys suspended in H_2O-based nanofluid or hybrid nanofluid flowing across a non-linear porous stretching sheet. Bhagyashri and Ashish [10] investigated the effects of slip states, thermal radiation, chemical reactions, and Cu-AA7075-AA7072/methanol trihybrid nanofluid flow over a spinning disc. Based on their consideration of heat sources and heat flux, Farooq et al. [11] examine the rates of heat transfer in hybrid nanofluid flows of (AA7075-AA7072/Methanol). As the thermal radiation parameters and Biot numbers increase, the temperature profiles also increase. Salhi et al. [12–18] analyze numerically the natural convection of nanofluids such as Al_2O_3, SiO_2, TiO_2, Cu, Ag, Al, Cu, and Al_2O_3 nanoparticles suspended in pure water with various geometries.

Zafar et.al [19] examined the effect of heat on 2D MHD boundary layer flow over a stretched sheet embedded in a porous medium. Using chemical manufacturing facilities and porous media, three-dimensional flow on a bilinearly expanding surface was studied by Padamavathi et al. [20-21]. In addition to other mass- and heat-transport phenomena, the impacts of thermal radiation and heat sources/sinks were examined in this study. The heat and mass transfer in 3D mixed-hollow-Darcy-Forchheimer bio-convection caused by Casson nanofluids passing through a stretched sheet was studied by Elhag [22]. As the magnetic and Forchheimer parameters increase, the velocities decrease. Nanofluid flow over a stretched surface with heat flux is studied in three dimensions by Zhang et al. [23] using the upper-converted Darcy-Forchheimer Maxwell model. Chemical processes, radiation, magnetic fields, Darcy-Forchheimer effects, heat production, and ferrofluid flows across a nonlinear stretching sheet were studied by Manjunatha et al. [24]. R^2 values for the output responses of derived quantities approached 1.0, showing high predictive accuracy of the statistical model. In a porous media that was stretched bilinearly, Manjunatha et al. [25–26] explored the thermal behavior of a Casson hybrid nanofluid. The impacts of a volumetric heat source/sink, chemical processes, and thermal radiation are multi-faceted. A decreasing concentration profile is associated with decreases in the chemical reaction parameter and the Schmidt number. The unstable mixed-mode high-pressure flow of a tetra hybrid nanofluid in a non-Darcy porous stretched cylinder is studied by Amudhini and Poulomi [27]. Furthermore, slip effects, chemical reactions, and heat generation are all factors to consider. The 3D Williamson fluid flow across a slip bidirectional extended flat horizontal surface is suggested in this dissertation and is investigated by Nasir et al. [28]. Raising the magnetic parameter causes the fluid flow to decrease. According to Veera Krishna [29-30], hybrid nanofluids may be considered when applied to a vertical porous surface that is experiencing exponential acceleration. It considers the Hall and ion-slip effects in the context of slip velocity in a rotating frame. The Sisko stretching surface bio-nanofluid flow in the presence of non-linear heat radiation was investigated by Eid et al. [31]. The effect of heat radiation on nanoparticle-laden Sisko nanofluid flow towards a stretched surface is studied by Hassan et al. [32]. The results show that the velocity profile decreases as the velocity-slip parameter increases. The Sisko slip bilinear stretching sheet was considered by Jyothi et al. [33]

2. Details of Sisko fluid rheological model

For a simple shear flow, the shear stress τ is related to the shear rate $\dot{\gamma}$ by

$$\tau = a\dot{\gamma} + b\dot{\gamma}^{n}$$

Parameters:

- τ = Shear stress
- $\dot{\gamma} = \left|\frac{\partial u}{\partial y}\right|$: Shear (strain) rate
- a: Newtonian viscosity coefficient (high-shear viscosity)
- b: Consistency index (non-Newtonian strength)
- n: power-law index
  - n<1: shear-thinning fluid
  - n=1: Newtonian fluid
  - n>1: Shear-thickening fluid

The clear viscosity μ_{app} is

$$\mu_{app} = a + b\dot{\gamma}^{n-1}$$

This shows that viscosity depends explicitly on the local strain rate

The extra stress tensor τ is written as

$$\tau = \left[a + b\left(\sqrt{\frac{1}{2}A_1 : A_1}\right)^{n-1}\right]A_1$$

Where,

- $A_1 = \nabla v + (\nabla v)^T$ is the first Rivlin-Ericksen tensor,
- $\sqrt{\frac{1}{2}A_1 : A_1}$ is the effective shear rate.

After non-depersonalization the momentum equation typically introduces a dimensional Sisko parameter B:

$$B = \frac{bU_0^{n-1}}{a\ L_0^{n-1}}$$

Where,

U_0 characteristic velocity, L: Characteristic length.

This parameter measures the size of non-Newtonian effects compared to Newtonian viscous effects.

The current findings are pertinent to practical systems that involve magnetic nanofluid transport, including thermal management devices, processing of porous materials, and energy conversion systems. Understanding how non-Newtonian behavior, magnetic control, and heat generation affect each other can help you improve the performance of industrial heat and mass transfer operations. The current model has theoretical significance and contributes to the development of advanced cooling and energy-efficient engineering systems.

This research fills a gap in literature by adopting a novel approach to a previously unstudied topic: the impact of several intricate, physically relevant phenomena on the flow of Sisko hybrid nanofluid over a bilinear stretching sheet. This research is unusual in that it includes the combined effects of heat and mass flow models, Darcy-Forchheimer effects, thermal radiation, magnetic fields, chemical processes, and heat production, rather than earlier efforts, which focus on isolated effects or simpler nanofluid models. To perfect current thermal management methods, it is necessary to understand flow behavior, thermal enhancement, and mass transfer. This may be achieved by using this comprehensive modelling approach in conjunction with a numerical solution that offers new insights into these areas. The nonlinear, coupled partial differential equations must first be reduced to ordinary differential equations (ODEs) using similarity transformations. We use the MATLAB bvp4c solver to compute the solutions. Tables and figures illustrate the effects of critical factors such as speed, temperature, concentration, and derived quantities. Using the response surface approach, the calculated shear stress and heat- and mass-transfer rates are examined.

3. Mathematical formulation

Here, a 3D MHD Sisko nano liquid is considered, together with a stretching sheet defined by $Uw = \frac{c_1 x}{1 - \beta t}$ velocities and $Vw = \frac{d_1 y}{1 - \beta t}$. Methanol is the base fluid of this nanofluid, which is composed of AA7072 and AA7075 nanoparticles. Figure 1 illustrates these situations. It is clear from observation that u stands for the speed along the x-axis, where $c_1 > 0$ means the stretching rate, and v stands for the speed along the y-axis, where $d_1 > 0$ means the stretching rate. The z-axis is the only degree of freedom available to the fluid, and it stays perpendicular to the surface. The data suggests that the nano-liquid has a higher temperature near the surface of the sheet. In addition, a magnetic field is B_0 applied from outside the system along the y-axis. Both the applied electric field and the induced magnetic field are disregarded. Furthermore, cross-diffusion effects (Soret and Dufour) are neglected, and the porous medium is assumed to be homogeneous and isotropic. Table 1 provides detailed information on the thermophysical properties of the nanoparticles and the base fluid. Given these assumptions, we may write the governing equations as Equations. (1)– (5), which include momentum, energy, and concentration variables, and account for variations in thermal conductivity and viscosity. [33, 24]

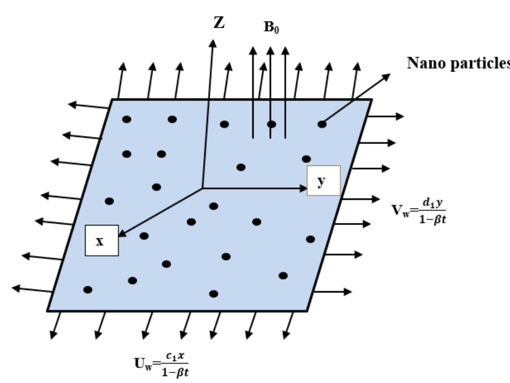

Figure 1. Geometry of the problem

$$u_x + v_y + w_z = 0 \tag{1}$$

$$uu_x + vu_y + wu_z = \frac{\mu_{hnf}}{\rho_{hnf}}\left(\mu(T)u_z\right)_z - \frac{b}{\rho_{hnf}}\left((-u_z)^n\right)_z - \frac{\sigma_{hnf}B_0^2}{\rho_{hnf}}u - \frac{C_b}{\sqrt{K_p}}u^2 \tag{2}$$

$$uv_x + vv_y + wv_z = \frac{\mu_{hnf}}{\rho_{hnf}}\left(\mu(T)v_z\right)_z - \frac{b}{\rho_{hnf}}\left((-u_z)^{n-1}\right)_z v_z - \frac{\sigma_{hnf}B_0^2}{\rho_{hnf}}v - \frac{C_b}{\sqrt{K_p}}v^2 \tag{3}$$

$$uT_x + vT_y + wT_z = \frac{k_{hnf}}{(\rho C_p)_{hnf}}\left(K(T)T_z\right)_z - \frac{1}{(\rho C_p)_{hnf}}(q_r)_z + \frac{Q_0}{(\rho C_p)_{hnf}}(T - T_\infty) \tag{4}$$

$$uC_x + vC_y + wC_z = D_B C_{zz} - K_1(C - C_\infty) \tag{5}$$

All parameters are defined in the notation section. The final terms in the momentum Equations (2) and (3) denote the Forchheimer inertial drag forces, and the penultimate terms denote the Lorentz magnetic body forces in the x and y directions. In the energy Equation (4), the penultimate term is the radiative heat flux term (Rosseland model) and the final term is the heat source/sink term. In the species diffusion Equation (5), the final term is the first-order homogeneous destructive chemical reaction term. We employ the Rosseland algebraic approximation.

By using Rosseland approximation,

$$q_r = -\frac{4\sigma^*}{3k^*}\left(T^4\right)_z \tag{6}$$

The Rosseland diffusion approximation assumes that the hybrid nanofluid medium is optically thick. In this case, radiative heat transfer occurs primarily by diffusion because the nanoparticles increase the medium's absorption of heat. The absorption coefficient is considered a useful, constant thermophysical property of the nanofluid.

Approximating with Taylor's Series, $T^4 \cong 4T_\infty^3 T - 3T_\infty^3$, Equation (4) changes to,

$$uT_x + vT_y + wT_z = \frac{k_{hnf}}{(\rho C_p)_{hnf}}\left(K(T)T_z\right)_z - + \frac{16\sigma^* T_\infty^3}{3(\rho C_p)_{hnf}k^*}T_{zz} + \frac{Q_0}{(\rho C_p)_{hnf}}(T - T_\infty)$$

The related boundary conditions are,

$$u = Uw + \frac{c_1 x}{1-\beta t}u_z, v = Vw + \frac{d_1 y}{1-\beta t}v_z, w = 0, T = T_w + \frac{c_1 x}{1-\beta t}T_z,$$
$$C = C_w + \frac{c_1 x}{1-\beta t}C_z\,(z=0)$$

$$u \to 0, v \to 0, T \to T_\infty, C \to C_\infty \tag{8}$$

The above nonlinear dimensional partial differential equation boundary-value problem, defined by Equations (1), (2), (3), (5) and (8) with boundary conditions (8), can be made into a nonlinear ordinary differential equation boundary-value problem by virtue of the following madding transformations:,

$$u = \frac{c_1 x}{1-\beta t}f'(\eta), v = \frac{d_1 y}{1-\beta t}g'(\eta), \eta = z\left(\frac{c^{n-2}\rho_f}{b}\right)^{\frac{1}{n+1}}x^{\frac{1-n}{1+n}}(1-\beta t)^{\frac{n-2}{n+1}}$$
$$w = -c_1\left(\frac{c^{n-2}\rho_f}{b}\right)^{\frac{1}{n+1}}\left(\frac{2n}{n+1}f(\eta) + \eta\left(\frac{1-n}{1+n}\right)f'(\eta) + g(\eta)\right)x^{\frac{n-1}{1+n}}(1-\beta t)^{\frac{1-2n}{n+1}}$$
$$\theta(\eta) = \frac{T - T_\infty}{T_w - T_\infty}, \phi(\eta) = \frac{C - C_\infty}{C_w - C_\infty} \tag{9}$$

Thermophysical characteristics for nanoparticles are computed with the following modified Tiwari-Das volume fraction relations: [34]

Thermophysical properties of hybrid nanoparticle and base fluid (methanol) are provided in

$$\left.\begin{aligned}
&\rho_{hnf} = (1-\phi_2)\left[(1-\phi_1)\rho_f + \phi_1\rho_{s1}\right] + \phi_2\rho_{s2},\\
&\mu_{hnf} = \frac{\mu_f}{(1-\phi_1)^{2.5}(1-\phi_2)^{2.5}},\\
&\frac{\sigma_{hnf}}{\sigma_{nf}} = \frac{\sigma_{s2} + 2\sigma_{nf} - 2\phi_2(\sigma_{nf} - \sigma_{s2})}{\sigma_{s2} + 2\sigma_{nf} + \phi_2(\sigma_{nf} - \sigma_{s2})}, \frac{\sigma_{nf}}{\sigma_f} = \frac{\sigma_{s1} + 2\sigma_f - 2\phi_1(\sigma_f - \sigma_{s1})}{\sigma_{s1} + 2\sigma_f + \phi_1(\sigma_f - \sigma_{s1})},\\
&(\rho C_p)_{hnf} = (1-\phi_2)\left[(1-\phi_1)(\rho C_p)_f + \phi_1(\rho C_p)_{s1}\right] + \phi_2(\rho C_p)_{s2},\\
&(\rho\beta)_{hnf} = (1-\phi_2)\left[(1-\phi_1)(\rho\beta)_f + \phi_1(\rho\beta)_{s1}\right] + \phi_2(\rho\beta)_{s2},\\
&\frac{k_{hnf}}{k_{nf}} = \frac{k_{s2} + 2k_{nf} - 2\phi_2(k_{nf} - k_{s2})}{k_{s2} + 2k_{nf} + \phi_2(k_{nf} - k_{s2})}, \frac{k_{nf}}{k_f} = \frac{k_{s1} + 2k_f - 2\phi_1(k_f - k_{s1})}{k_{s1} + 2k_f + \phi_1(k_f - k_{s1})},
\end{aligned}\right\} \tag{10}$$

Table 1. Thermophysical characteristics of nanoparticle base fluids [35]

	Base fluid	Ferro particles	
	Methanol		AA7075
ρ (kg/m^3)	792	2720	2810
C_p(J/kgK)	2545	893	960
k(W/mK)	0.2035	222	173
σ (Um^{-2})	0.5 x 10^{-6}	34.84 x 10^6	26.77 x 10^6

Here all parameters are defined in the nomenclature. The emerging dimensionless governing equations (wherein mass conservation is automatically satisfied) assume the forms:

$$\frac{A_1}{A_2}B\left((1+\varepsilon\theta)f'''(\eta) + \varepsilon\theta'(\eta)f''(\eta)\right) - \frac{B_n}{A_2}\left(-f''(\eta)\right)^{n-1}f'''(\eta) - \frac{A_3}{A_2}Mf'(\eta)$$
$$+\left(\frac{2n}{n+1}f(\eta) + g(\eta)\right)f''(\eta) - (1+Fr)f'(\eta)^2 = 0 \tag{11}$$

$$\frac{A_1}{A_2}B\left((1+\varepsilon\theta)g'''(\eta) + \varepsilon\theta'(\eta)g''(\eta)\right) - \frac{B_n}{A_2}\left(-f''(\eta)\right)^{n-1}f'''(\eta)g''(\eta) - \frac{A_3}{A_2}Mg'(\eta)$$
$$+\left(\frac{2n}{n+1}f(\eta) + g(\eta)\right)g''(\eta) - (1+Fr)g'(\eta)^2 = 0 \tag{12}$$

$$\frac{A_4}{A_5}\left((1+\varepsilon\theta)\theta''(\eta) + \varepsilon\theta'(\eta)\right) + \frac{R}{A_5}\theta''(\eta) + Pr\left(\frac{2n}{n+1}f(\eta) + g(\eta)\right)\theta'(\eta)$$
$$-Prf'(\eta)\theta(\eta) + \frac{PrQ}{A_5}\theta'(\eta) = 0 \tag{13}$$

$$\phi''(\eta) - ScKr\phi(\eta) - Sc\phi(\eta)f'(\eta) + Sc\left(\frac{2n}{n+1}f(\eta) + g(\eta)\right)\phi'(\eta) = 0 \tag{14}$$

The dimensionless boundary conditions become:

$$f(0) = V_0,\ f'(0) = 1 + \lambda f''(0),\ g'(0) = 1 + \gamma g''(0),\ g(0) = 0,\ \theta(0) = 1 + \beta\theta'(0),$$
$$\phi(0) = 1 + \xi\phi'(0),\ f'(\infty) \to 0,\ g'(\infty) \to 0,\ \theta(\infty) \to 0,\ \phi(\infty) \to 0 \tag{15}$$

Here the following dimensionless parameters arise:

$$B = \frac{Re_b^{\frac{2}{n+1}}}{Re_a},\ R = \frac{16T_\infty^3\sigma^*}{3k^*k_f},\ M = \frac{\sigma_f B_0^2}{\rho_f}\left(\frac{1-\beta t}{c_1}\right),\ \lambda = \left(\frac{c_1}{1-\beta t}\right)Re_b^{\frac{1}{n+1}},$$
$$\gamma = \left(\frac{d_1}{1-\beta t}\right)Re_b^{\frac{1}{n+1}},$$
$$\xi = \left(\frac{c_1}{1-\beta t}\right)^2\frac{Re_b^{\frac{1}{n+1}}}{(T_w - T_\infty)},\ \beta = \left(\frac{c_1}{1-\beta t}\right)^2\frac{Re_b^{\frac{1}{n+1}}}{(C_w - C_\infty)},\ Fr = \frac{C_b}{\sqrt{K_p}}\left(\frac{1-\beta t}{c_1}\right)^2,$$
$$Kr = K_1\left(\frac{1-\beta t}{c_1}\right),\ Q = \frac{Q_0}{(\rho C_p)_f},\ Pr = \frac{\mu_f C_{Pf}}{k_f} \tag{16}$$

The following essential parameters in this domain can be described: the skin-friction coefficients in the x and y directions, the local Nusselt number (Nu), and the local Sherwood number (Sh).

$$Cf = \frac{2\tau_{xz}}{\rho_f U_w^2},\ Cg = \frac{2\tau_{yz}}{\rho_f V_w^2},\ Nu = -\frac{xq_w}{(T_w - T_\infty)} T_z\big|_{z=0},\ Nu = -\frac{xj_w}{(C_w - C_\infty)} C_z\big|_{z=0} \tag{17}$$

Where, $\tau_{xz} = (a + b|u_z|^{n-1})u_z, \tau_{yz} = (a + b|v_z|^{n-1})v_z$

$$\frac{1}{2}Re_b^{\frac{1}{n+1}}Cf = Bf'(0) - [(-f'(0))]^n,\ Re^{-\frac{1}{n+1}}Nu = -\theta'(0),$$
$$\frac{1}{2}Re_b^{\frac{1}{n+1}}Cg = \frac{V_w}{U_w}[Ag''(0) + [(-f'(0))^{n-1}g''(0)]^n],\ Re^{-\frac{1}{n+1}}Sh = -\phi'(0) \tag{18}$$

4. Numerical procedure

Exact solutions for the boundary value problem defined by Equations (11)-(14) under boundary conditions (15) are intractable due to coupling and non-linearity. Therefore, the use of a numerical method is necessary. The MATLAB-based BVP4C approach for first-order first value problems is useful. First, the multi-degree, multi-order differential equations are reduced to first order to ease solving the equations (11)-(14). Appropriate substitutions are deployed, and a shooting technique is used in BVP4C as follows [36].

$$\left.\begin{aligned} &f(\eta) = \Psi_1,\ f'(\eta) = \Psi_2,\ f''(\eta) = \Psi_3,\ f'''(\eta) = \Psi_3',\\ &g(\eta) = \Psi_4,\ g'(\eta) = \Psi_5,\ g''(\eta) = \Psi_6,\ g'''(\eta) = \Psi_6',\\ &\theta(\eta) = \Psi_7,\ \theta'(\eta) = \Psi_8,\ \theta''(\eta) = \Psi_8',\\ &\phi(\eta) = \Psi_9,\ \phi'(\eta) = \Psi_{10},\ \phi''(\eta) = \Psi_{10}', \end{aligned}\right\} \tag{19}$$

$$\Psi_3' = \frac{\frac{A_3}{A_2}M\Psi_2 - \left(\frac{2n}{n+1}\Psi_1 + \Psi_4\right)\Psi_3 + (1 + Fr)\Psi_2^2 - \frac{A_1}{A_2}B\varepsilon\Psi_8\Psi_3}{\frac{A_1}{A_2}B(1 + \varepsilon\Psi_7) - \frac{B_n}{A_2}(-\Psi_3)^{n-1}} \tag{20}$$

$$\Psi_6' = \frac{\frac{A_3}{A_2}M\Psi_5 - \left(\frac{2n}{n+1}\Psi_1 + \Psi_4\right)\Psi_6 + (1 + Fr)\Psi_5^2 - \frac{A_1}{A_2}B\varepsilon\Psi_8\Psi_6 + \frac{B_n}{A_2}(-\Psi_3)^{n-1}\Psi_3'\Psi_6}{\frac{A_1}{A_2}B(1 + \varepsilon\Psi_7)} \tag{21}$$

$$\Psi_8' = \frac{-Pr\left(\frac{2n}{n+1}\Psi_1 + \Psi_4\right)\Psi_8 + Pr\Psi_2\Psi_7 - \frac{PrQ}{A_5}\Psi_7 - \frac{A_4}{A_5}\varepsilon\Psi_8}{\frac{A_4}{A_5}(1 + \varepsilon\Psi_7) + \frac{R}{A_5}} \tag{22}$$

$$\Psi_{10}' = ScKr\Psi_9 + Sc\Psi_9\Psi_2 - Sc\left(\frac{2n}{n+1}\Psi_1 + \Psi_4\right)\Psi_9 \tag{23}$$

$$\begin{aligned} &\Psi_0(1) = V_0,\ \Psi_0(2) = 1 + \lambda\Psi_0(3),\ \Psi_0(5) = 1 + \gamma\Psi_0(6),\ \Psi_0(4) = 0,\ \Psi_0(7) = 1 + \xi\Psi_0(8),\\ &\Psi_0(9) = 1 + \beta\Psi_0(9),\ \Psi_1(2) \to 0,\ \Psi_1(5) \to 0,\ \Psi_1(7) \to 0,\ \Psi_1(9) \to 0 \end{aligned} \tag{24}$$

The code is confirmed against previously published computations reported by Jyothi et al. [33] for M (magnetic interaction parameter) and B (Sisko parameter) values in the absence of Fr (Forchheimer effect) and Q (heat source/sink). The outcomes $-f''(0)$ for axial skin friction are well matched, as saw in Table 2, and confidence in the MATLAB BVP4C procedure is therefore justifiably high.

Table 2. Skin friction comparison for φ, M, Pr and B. Pr=28, R=0.5, Kr = 0.1, $\beta = \gamma = \lambda = V_0 = 0.5$.

Parameters			$-f''(0)$		
φ	M	B	Jyothi et al. [33]	Current work	Percentage error
0.01	0.5	1	0.64368	0.64372	0.00621 %
0.05	0.5	1	0.46756	0.46751	0.01070 %
0.1	0.5	1	0.25719	0.25724	0.01740 %
0.01	0.8	1	2.85496	2.85488	0.00280 %
0.01	1.2	1	4.52842	4.52850	0.00177 %
0.01	0.5	1	2.92436	2.92441	0.00171 %
0.01	0.5	2	1.92671	1.92666	0.00259 %
0.01	0.5	3	1.51711	1.51705	0.00396 %

5. Result and discussion

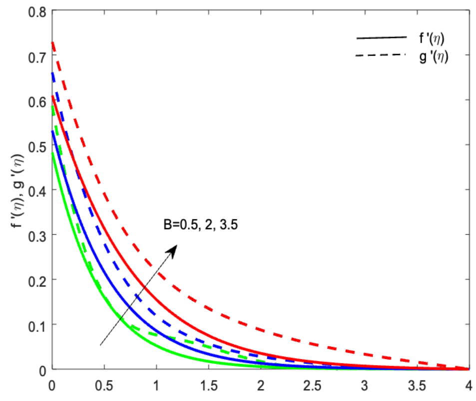

(a)

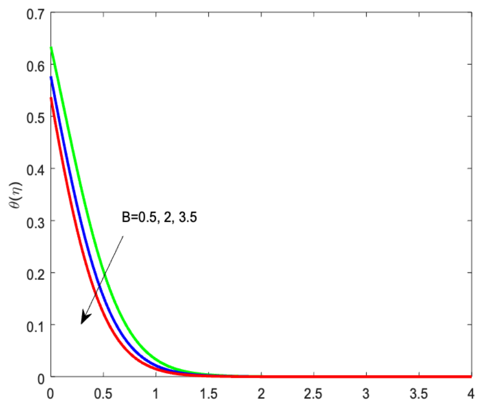

(b)

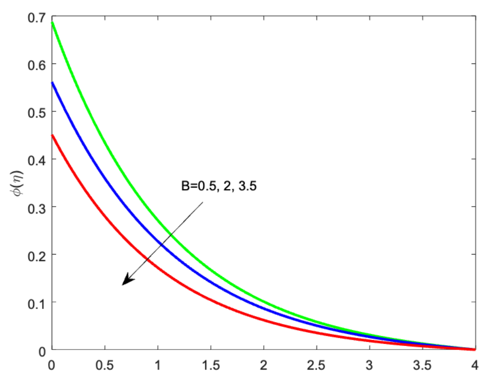

(c)

Figure 2. Influence of Sisko fluid parameter on **(a)** radial and transverse velocity, **(b)** temperature and **(c)** concentration

A graphical representation of material characterization proving the relationship between fluid velocity and the Sisko fluid parameter is shown in Figure 2(a). As proved in the illustration, both parameters are correlated, which may be attributable to the inverse relationship between the material parameter (B) and viscosity. Results from this study suggest that decreasing fluid viscosity, extension, and resistance to fluid motion raises the Sisko parameter. This causes a rise in fluid velocity. The effect of the material property, represented by the Sisko fluid parameter B, on the fluid temperature and concentration is shown graphically in Figure 2(b-c). A Negative relationship between increases in B and decreases in fluid temperature and concentration appears to be the observed trend. Increasing the Sisko parameter reduces the effective viscosity in shear-thinning regimes; this reduction enhances flow velocity but simultaneously diminishes viscous dissipation. The reduced internal friction lowers heat generation, while stronger convection enhances heat removal, leading to an overall decrease in temperature.

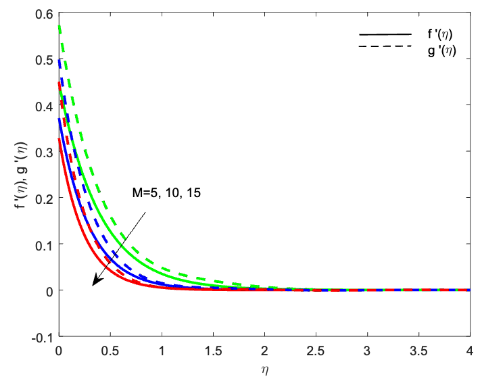

(a)

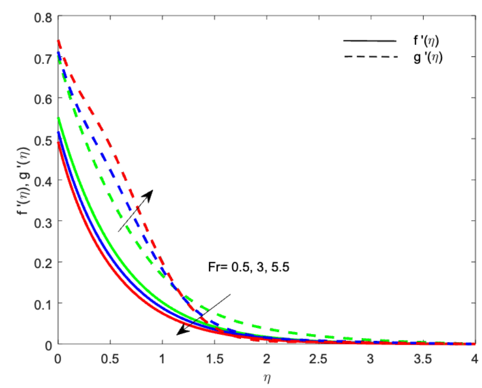

(b)

Figure 3. Influence of velocity on **(a)** magnetic parameter and **(b)** Darcy-Forchheimer

As the value of the magnetic parameter increases, the dimensionless velocity of the nanofluid decreases, as shown in Figure 3(a). The combination of an electric current and a magnetic field creates a Lorentz force that reduces fluid velocity. This impact is amplified by increasing magnetic parameters, which further reduce fluid velocity. The thickness of the velocity boundary layer is almost unaffected by a decrease in velocity, since it is governed by the ratio of inertial to viscous forces in the fluid, which is unaffected by changes in magnetic parameters. Hence, the velocity was reduced by the Lorentz force without affecting the boundary-layer thickness. The interactions between AA7072 and AA7075 nanoparticles are further influenced by the viscosity and other distinctive rheological characteristics of the hybrid nanofluids. Magnetite, when subjected to magnetic fields, offers further control over the rheological behavior of the fluid via the magneto-rheological effect, while AA7072 imparts shear-thinning behavior and increases viscosity. Taken as a whole, these features affect the flow dynamics and dimensionless velocity of these nanofluids, which in turn affect their response to magnetic fields. The velocity profile for a Darcy-Forchheimer flow, plotted against the dimensionless variable, is shown in Figure 3(b). The velocity decreases beyond the point of loss of stability at a transverse velocity of 1, while it increases within the range of 0 to 1. The velocity profile becomes flatter as Fr rises. The thickness within the boundary layer decreases as Fr rises. This action is helpful when reducing wall drag is necessary. Overall, the Forchheimer parameter (Fr) is the nonlinear drag characteristics of a porous medium. Increases in the Forchheimer parameter (Fr) are expected to lead to more energy dissipation owing to inertial effects, which is consistent with the observed drop in velocity. This behavior aligns with the findings of Jyothi et al. [33] and Sohail et al. [4], both of whom noted a velocity increase corresponding to a rising Sisko parameter. The current findings augment their research by incorporating Darcy-Forchheimer resistance and the effects of hybrid nanoparticles.

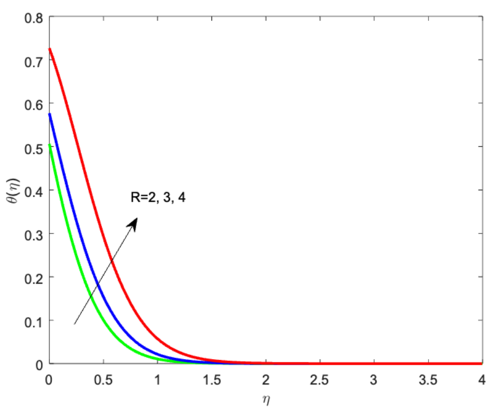

(a)

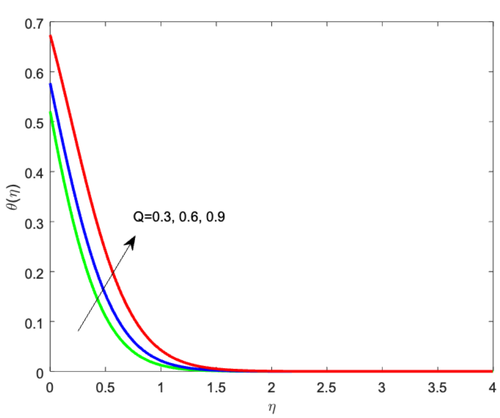

(b)

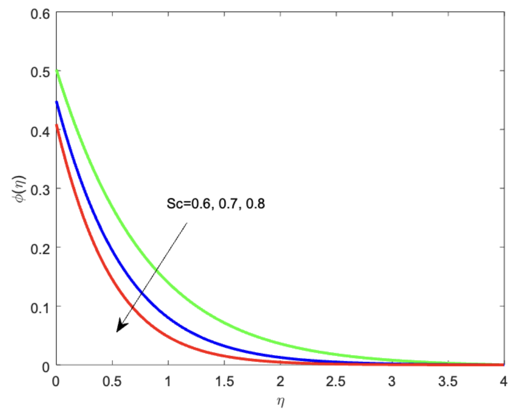

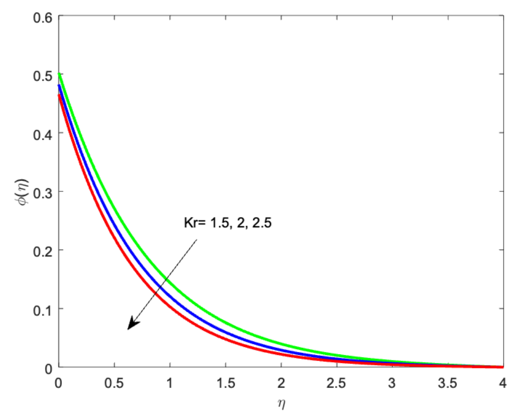

Figure 4. Influence of temperature effect on **(a)** thermal radiation **(b)** heat source

The rise in Figure 4(a), which depicts temperature fluctuations for different values of the radiation parameter R, shows an increase in temperature. A higher value of the radiation parameter (R) leads to an elevated temperature profile. The rising relative importance of radiative and convective heat transport causes this effect to materialize. One of the most important mechanisms for raising temperature is radiative heat transfer, because it does not require a physical medium. An increase in R steepens the boundary-layer temperature gradient and thereby thickens the boundary layer. Radiative heat transfer plays an increasingly large role in the system as the radiation parameter (R) increases, leading to increased temperature. Improvement in thermal dispersion is observed as the heat generation parameter increases (Figure 4 (b)). It measures the amount of heat is produced per unit mass or per unit volume of the fluid. Q is a measure of the fluid's internal heat production, which affects its flow behavior and temperature distribution. The rise in temperature caused by thermal radiation aligns with earlier numerical studies on radiative nanofluid flows [13, 24], confirming that radiation increases thermal boundary layer thickness.

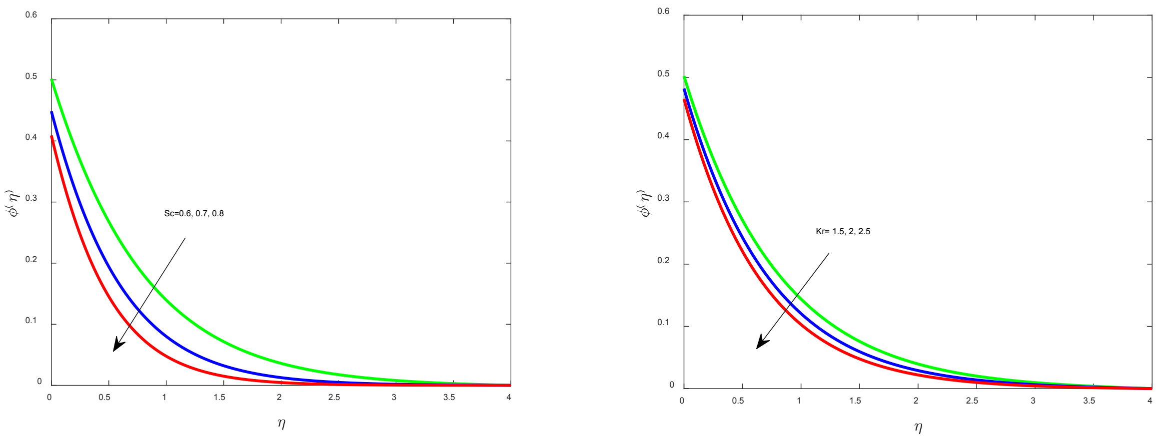

(a) **(b)**

Figure 5. Influence of concentration on **(a)** Schmidt number and **(b)** chemical reaction

Figure 5(a) shows effect of the Schmidt number Sc on the distribution of concentrations. Mass diffusivity is low for large Sc values. A mathematical representation of fluid flow is obtained by expressing the Schmidt number as a dimensionless ratio relating mass diffusivity to momentum diffusivity. In physical terms, these two concepts are known as the mass-transfer layer and the hydrodynamic-thickness layer, respectively. A reduction in the concentration field and an increase in the Schmidt factor result from decreased mass diffusion. Figure 5(b) proves properties of the chemical reaction and its impact on concentration. Raising this parameter causes a decrease in the nanofluid concentration. The decrease in concentration as the Schmidt number rises corresponds to proposed transfer of mass theory and corroborates earlier hybrid nanofluid research [18,26].

6. Response surface method

Response Surface Methodology (RSM) is an excellent tool for deciding on empirical relationships among several constraints. Its capacity to analyses how input elements influence output makes it extremely useful for the evaluation of multivariate processes. The impact of skin friction, Sherwood number, Sc, Kr, B, Nusselt number, R, and Q was investigated in this work, using RSM. M, Fr, and B are the parameters being examined. Tables 3, 7, and 10 show the results of a three-level variation in the input parameters within the stated ranges. [30-31]

After choosing the inputs, a statistical model was built and run 20 times, as shown in Tables 4, 8, and 11. To show the interaction between inputs and solution, a second-order multinomial is used.

A second order polynomial was used to construct the model with intercept represented by J_0, the linear J_i, the quadratic J_{ii}, and the interaction J_{ij}. The regression coefficients show the correlation between the input parameters; this correlation affects the terms. To fit this polynomial, the CCD is employed. This configuration allows 20 runs. Design architecture eases more efficient factor space exploration and makes it simpler to estimate the polynomial model's regression coefficients.

Table 3. Impacts of different Skin friction parameter settings

Parameter	Symbol	Level		
		-1	0	+1
$5 \leq M \leq 15$	W_1	5	10	15
$0.5 \leq Fr \leq 5.5$	W_2	0.5	3	5.5
$0.5 \leq B \leq 3.5$	W_3	0.5	2	3.5

$$Cf = J_0 + J_1 M + J_2 Fr + J_3 B + J_{11} M^2 + J_{22} Fr^2 + J_{33} B^2 + J_{12} M * Fr + J_{13} M * B + J_{14} Fr * B$$

Table 4. A CCD-based investigative approach

Runs	Coded values			Real values			Response	
	W_1	W_2	W_3		Fr	B	Cf	Cg
1	-1	-1	-1	5	5.5	3.5	2.59499	3.46355
2	1	-1	-1	15	5.5	3.5	2.74877	3.75561
3	-1	1	-1	10	3	0.5	0.324217	0.455028
4	1	1	-1	5	0.5	0.5	0.329646	0.429432
5	-1	-1	1	10	3	2	1.29696	1.81994
6	1	-1	1	10	0.5	2	1.29316	1.82919
7	-1	1	1	10	3	2	1.29696	1.81994
8	1	1	1	10	3	3.5	2.26969	3.18485
9	-1	0	0	10	3	2	1.29696	1.81994
10	1	0	0	15	3	2	1.5677	2.13801
11	0	-1	0	10	5.5	2	1.30064	1.81469
12	0	1	0	10	3	2	1.29696	1.81994
13	0	0	-1	15	5.5	0.5	0.392651	0.536548
14	0	0	1	5	0.5	3.5	2.30771	3.00553
15	0	0	0	5	3	2	1.33041	1.70799
16	0	0	0	10	3	2	1.29696	1.81994
17	0	0	0	15	0.5	3.5	2.73811	3.72698
18	0	0	0	5	5.5	0.5	0.370671	0.494862
19	0	0	0	15	0.5	0.5	0.391129	0.532459
20	0	0	0	10	3	2	1.29696	1.81994

$$Cf = 1.2918 + 0.0905M + 1.0851B + 0.1649M^2 + 0.0626M * B$$

The suggested model is confirmed by analysis of variance (ANOVA) to ensure that it is applicable and has real-world implications. The outcomes are shown in Table 5. A given parameter is significant if its p-value is < 0.05. In other places, they aren't given much thought. The variables B, M^2, Fr^2, M*Fr, and Fr*B do not appear to be relevant. A score of 99.64% shows that the model is correct. This finding is based on examination of the data: the x-axis values for skin friction correspond to the input values (M, Fr, and B).

Table 5. ANOVA of Cf

Source	Degrees of freedom	Adjusted sum of squares	Adjusted mean squares	F-value	p-value	Coefficient
Model	9	12.0842	1.3427	308.50	0.000	
Linear	3	11.8683	3.9561	908.96	0.000	1.2918
M	1	0.0819	0.0819	18.82	0.001	0.0905
Fr	1	0.0121	0.0121	2.78	0.126	0.0348
B	1	11.7743	11.7743	2705.29	0.000	1.0851
Square	3	0.1639	0.0546	12.55	0.001	
M*M	1	0.0748	0.0748	17.18	0.002	0.1649
Fr*Fr	1	0.0004	0.0004	0.10	0.755	0.0127
B*B	1	0.0005	0.0005	0.10	0.754	0.0128
2-Way Interaction	3	0.0520	0.0173	3.98	0.042	
M*Fr	1	0.0125	0.0125	2.87	0.121	-0.0395
M*B	1	0.0313	0.0313	7.20	0.023	0.0626
Fr*B	1	0.0082	0.0082	1.87	0.201	0.0319
Error	10	0.0435	0.0044			
Lack-of-Fit	5	0.0435	0.0087	*	*	
Pure Error	5	0.0000	0.0000			
Total	19	12.1277				

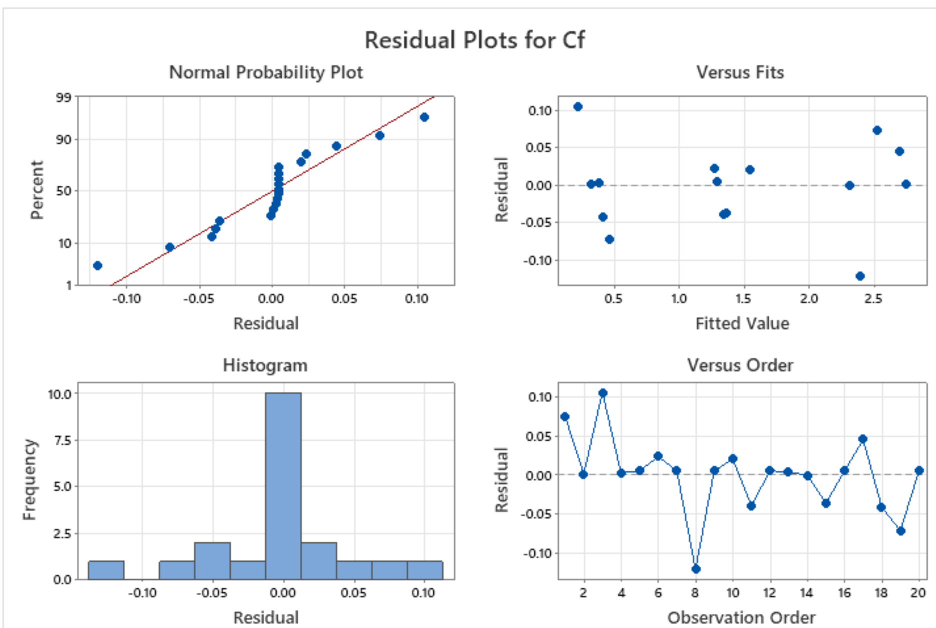

Figure 6. Residual versus observation for Cf

$$Cg = 1.81 + 0.1588M + 1.4688B + 0.1278M^2 + 0.1086M * B$$

We employ analysis of variance (ANOVA) to ensure that the given model is useful, and its effects are meaningful in real-world contexts. The findings are shown in Table 6. If the p-value of a parameter is less than 0.05, the parameter is considered important. They are not considered important elsewhere. The variables Fr, Fr^2, B^2, M*Fr, and Fr*B do not appear to be relevant. A score of 99.71% proves that the model is correct. This finding results from an examination of the data: the y-axis values of skin friction are related to the input variables (M, Fr, and B).

Table 6. ANOVA of Cg

Source	Degrees of freedom	Adjusted sum of squares	Adjusted mean squares	F-value	p-value	Coefficient

Model	9	22.1340	2.4593	388.69	0.000	
Linear	3	21.8559	7.2853	1151.43	0.000	1.8100
M	1	0.2523	0.2523	39.87	0.000	0.1588
Fr	1	0.0293	0.0293	4.64	0.057	0.0542
B	1	21.5743	21.5743	3409.77	0.000	1.4688
Square	3	0.1319	0.0440	6.95	0.008	
M*M	1	0.0449	0.0449	7.10	0.024	0.1278
Fr*Fr	1	0.0020	0.0020	0.31	0.589	0.0268
B*B	1	0.0017	0.0017	0.27	0.617	0.0248
2-Way Interaction	3	0.1462	0.0487	7.70	0.006	
M*Fr	1	0.0301	0.0301	4.76	0.054	-0.0613
M*B	1	0.0944	0.0944	14.91	0.003	0.1086
Fr*B	1	0.0217	0.0217	3.44	0.093	0.0521
Error	10	0.0633	0.0063			
Lack-of-Fit	5	0.0633	0.0127	*	*	
Pure Error	5	0.0000	0.0000			
Total	19	22.1972				

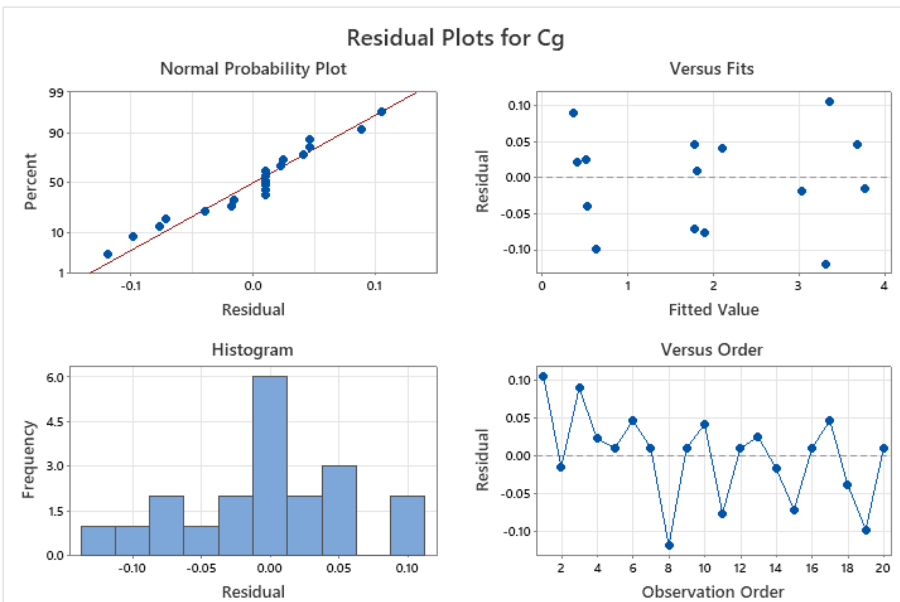

Figure 7. Residual versus observation for Cg

Table 7. Impact of different Nusselt number parameter settings

Parameter	Symbol	Level		
		-1	0	+1
$2 \leq R \leq 4$	W_1	2	3	4
$0.3 \leq Q \leq 0.9$	W_2	0.3	0.6	0.9
$0.5 \leq B \leq 3.5$	W_3	0.5	2	3.5

$$Nu = J_0 + J_1 R + Z_2 Q + J_3 B + J_{11} R^2 + J_{22} Q^2 + J_{33} B^2 + J_{12} R * Q + J_{13} R * B + J_{14} Q * B$$

Table 8. A CCD-based investigative approach

Runs	Coded values			Real values			Response
	W_1	W_2	W_3	R	Q	B	Nu
1	-1	-1	-1	4	0.9	0.5	1.02458
2	1	-1	-1	3	0.6	2	0.701779
3	-1	1	-1	2	0.3	0.5	1.00359
4	1	1	-1	3	0.3	2	1.00272
5	-1	-1	1	3	0.6	2	0.701779
6	1	-1	1	3	0.9	2	1.02524
7	-1	1	1	4	0.6	2	0.700639
8	1	1	1	2	0.6	2	0.703656
9	-1	0	0	3	0.6	2	0.701779
10	1	0	0	3	0.6	2	0.701779
11	0	-1	0	3	0.6	2	0.701779
12	0	1	0	4	0.9	3.5	1.02394
13	0	0	-1	2	0.9	0.5	1.02791
14	0	0	1	3	0.6	3.5	0.701732
15	0	0	0	3	0.6	0.5	0.702264
16	0	0	0	4	0.3	0.5	1.0025
17	0	0	0	4	0.3	3.5	1.02726
18	0	0	0	2	0.9	3.5	1.02394
19	0	0	0	3	0.6	2	0.701779
20	0	0	0	2	0.3	3.5	1.00338

The relevance and usefulness of the model are confirmed by ANOVA results. The outcomes are listed in Table 9. Statistical significance for the parameter is shown when the p-value is less than 0.05. R, B, R^2 and B^2 do not seem to have any statistical significance. The Accuracy of the model is proved by the R-value of 99.98%. The relationship between inputs (R, Q, B) and the Nusselt number is shown by data analysis.

Table 9. ANOVA of Nu

Source	Degrees of freedom	Adjusted sum of squares	Adjusted mean squares	F-value	p-value	Coefficient
Model	9	0.496008	0.055112	4754.29	0.000	
Linear	3	0.000807	0.000269	23.21	0.000	0.70141
R	1	0.000027	0.000027	2.33	0.158	0.00164
Q	1	0.000742	0.000742	64.04	0.000	0.00562
B	1	0.000038	0.000038	3.25	0.102	0.00194
Square	3	0.494909	0.164970	14231.28	0.000	
R*R	1	0.000005	0.000005	0.40	0.540	0.00130
Q*Q	1	0.269648	0.269648	23261.48	0.000	0.31314
B*B	1	0.000004	0.000004	0.32	0.587	0.00115
2-Way Interaction	3	0.000292	0.000097	8.39	0.004	
R*Q	1	0.000085	0.000085	7.36	0.022	-0.00326
R*B	1	0.000100	0.000100	8.64	0.015	0.00354
Q*B	1	0.000106	0.000106	9.17	0.013	-0.00364
Error	10	0.000116	0.000012			
Lack-of-Fit	5	0.000116	0.000023	*	*	
Pure Error	5	0.000000	0.000000			
Total	19	0.496124				

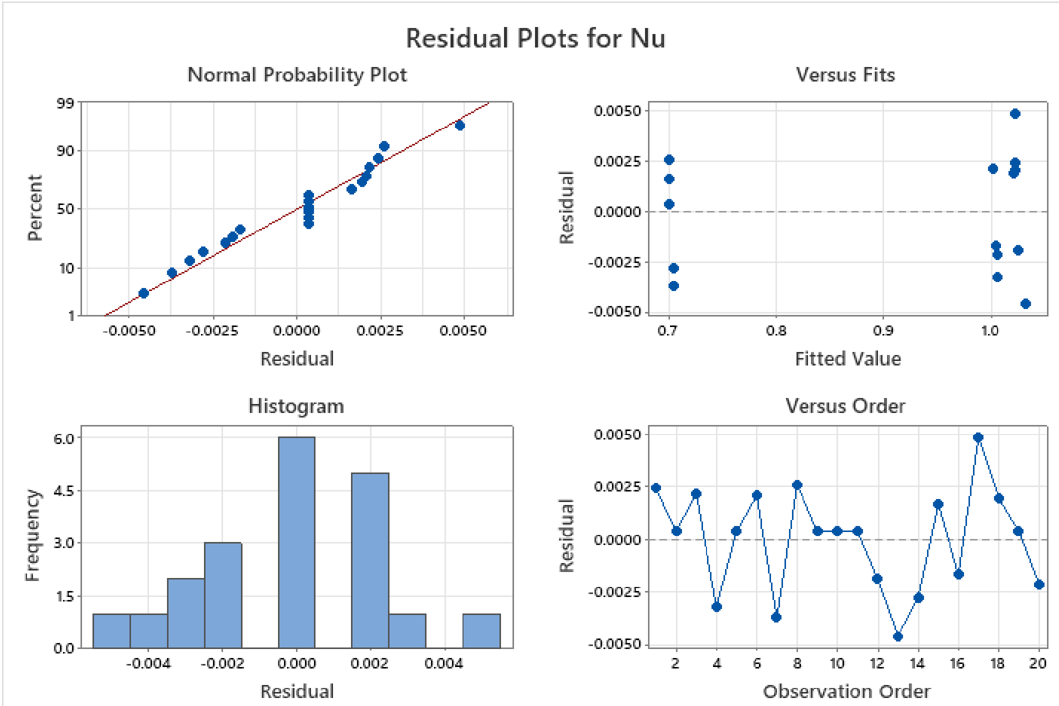

Figure 8. Residual vs. observation for Nu

Table 10. Impacts of different Sherwood number parameter settings

Parameter	Symbol	Level		
		-1	0	+1
$0.6 \leq Sc \leq 0.8$		0.6	0.7	0.8
$1.5 \leq Kr \leq 2.5$		1.5	2	2.5
$0.5 \leq B \leq 3.5$		0.5	2	3.5

$$Sh = J_0 + J_1 Sc + J_2 Kr + J_3 B + J_{11} Sc^2 + J_{22} Kr^2 + J_{33} B^2 + J_{12} Sc * Kr + J_{13} Sc * B + J_{14} Kr * B$$

Table 11. A CCD-based investigative approach

Runs	Coded values			Real values			Response
	W_1	W_2	W_3	Sc	Kr	B	Sh
1	-1	-1	-1	0.7	2	2	0.79695
2	1	-1	-1	0.8	2	2	0.830876
3	-1	1	-1	0.6	2	2	0.758406
4	1	1	-1	0.6	1.5	0.5	0.703066
5	-1	-1	1	0.7	2	2	0.79695
6	1	-1	1	0.7	2	2	0.79695
7	-1	1	1	0.7	2	2	0.79695
8	1	1	1	0.8	2.5	0.5	0.876935
9	-1	0	0	0.6	1.5	3.5	0.70305
10	1	0	0	0.8	2.5	3.5	0.876923
11	0	-1	0	0.6	2.5	0.5	0.803848
12	0	1	0	0.7	1.5	2	0.740911
13	0	0	-1	0.7	2	3.5	0.796949
14	0	0	1	0.7	2.5	2	0.842784
15	0	0	0	0.7	2	0.5	0.796963
16	0	0	0	0.8	1.5	0.5	0.774441

17	0	0	0	0.7	2	2	0.79695
18	0	0	0	0.7	2	2	0.79695
19	0	0	0	0.6	2.5	3.5	0.803837
20	0	0	0	0.8	1.5	3.5	0.774424

$$Sh = 0.796947 + 0.036139Sc + 0.050844Kr - 0.002301Sc^2 - 0.005095Kr^2 + 0.000428Sc * Kr$$

Table 12. ANOVA of Sh

Source	Degrees of freedom	Adjusted sum of squares	Adjusted mean squares	F-value	p-value	Coefficient
Model	9	0.039139	0.004349	971585.68	0.000	
Linear	3	0.038911	0.012970	2897815.83	0.000	0.796947
Sc	1	0.013060	0.013060	2917939.89	0.000	0.036139
Kr	1	0.025851	0.025851	5775507.48	0.000	0.050844
B	1	0.000000	0.000000	0.11	0.748	-0.000007
Square	3	0.000226	0.000075	16832.07	0.000	
Sc*Sc	1	0.000015	0.000015	3254.04	0.000	-0.002301
Kr*Kr	1	0.000071	0.000071	15948.40	0.000	-0.005095
B*B	1	0.000000	0.000000	0.11	0.742	0.000014
2-Way Interaction	3	0.000001	0.000000	109.14	0.000	
Sc*Kr	1	0.000001	0.000001	327.41	0.000	0.000428
Sc*B	1	0.000000	0.000000	0.00	0.992	-0.000000
Kr*B	1	0.000000	0.000000	0.00	0.959	0.000001
Error	10	0.000000	0.000000			
Lack-of-Fit	5	0.000000	0.000000	*	*	
Pure Error	5	0.000000	0.000000			
Total	19	0.039139				

After examining the suggested model and its real-world effects using ANOVA, we have the output is documented in Table 12. Sc*B, Kr*B, B*B, and B*B are not statistically significant. A model is considered valid when its R^2 score is 100%. A comprehensive statistical investigation confirms the correlation between the inputs (Sc, Kr, B) and the Sherwood numbers.

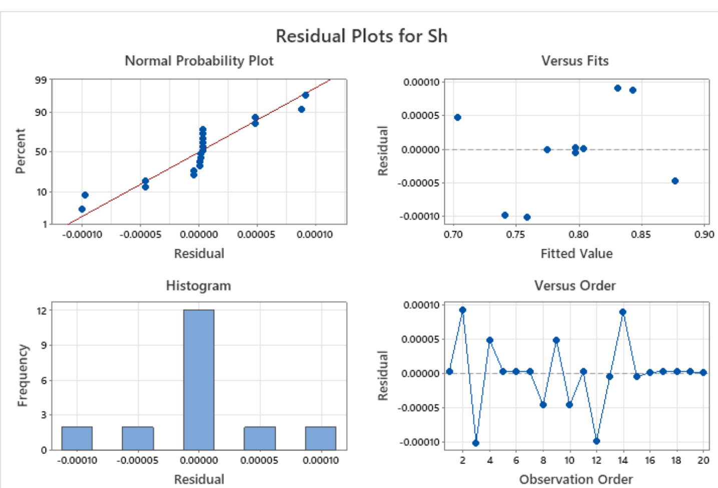

Figure 9. Residual vs. observation for Nu

The study's residual plots for Cf, Cg, Nu, and Sh are displayed in Figures 6, 7, 8, and 9. The regression probability plot reveals that the residuals are normally distributed. No discernible pattern is clear in the distribution of the residuals shown in the histogram. An appealing arrangement has been made with the largest remnants. Conversely, the overall trend and residual distribution show that the proposed model is effective and provides an excellent fit. The quadratic model developed in this study accurately captures the variations in the response variables Cf, Cg, Nu, and Sh.

7. Conclusion

The mixed-mode MHD Forchheimer flow of a Sisko hybrid nanofluid, with AA7072–AA7075 nanoparticles dispersed in methanol, over a bilinear stretching sheet was analyzed, accounting for slip and convective boundary conditions. The numerical results proved that increasing the Sisko parameter enhanced the radial and transverse velocity components, while the temperature and concentration profiles decreased. Stronger magnetic and Darcy–Forchheimer parameters reduced fluid velocity, while thermal radiation and heat source parameters increased temperature distribution. Furthermore, concentration profiles decreased with increasing Schmidt number and with intensified chemical reaction effects. The high R^2 values obtained from the response surface analysis confirmed the accuracy, robustness, and reliability of the proposed models. The information gained from this study can be used in advanced cooling systems, the processing of magnetic materials, and energy technologies that use hybrid nanofluids. These results support the creation of effective ways to control temperature in modern engineering applications

8. Future work

- Sisko hybrid nanofluid flow over a bi-linear stretching sheet with different boundary conditions.
- First-grade(or)Williamson(or)Carrie nanofluids with nonlinear thermal radiation effects flow over exponential, linear, cylindrical, cone, and wedge stretching surfaces.

Author contributions statement

Nirisha: Conceptualization, Methodology, Software, Formal Analysis, Investigation, Data Curation, Visualization, Writing – Original Draft Preparation. Nagaradhika: Validation, Supervision, Methodology, Writing – Review & Editing, Interpretation of Results, Resources, Final Approval of the Manuscript. Manjunath: Supervision, Software Implementation, Writing – Review & Editing, Funding Acquisition. All authors have read and approved the final version of the manuscript and agree to be accountable for all aspects of the work.

Funding

The authors received no financial support from any funding agency for the research, authorship, and/or publication of this article.

Data availability statement

All data generated or analyzed during this study are included in this published article. Additional data are available from the corresponding author upon reasonable request.

Declaration

The authors declare that this manuscript is original and has not been published previously, nor is it under consideration for publication elsewhere.

Declaration of generative AI and AI-assisted technologies in the writing process

The authors declare that no generative AI or AI-assisted technologies were used in the writing, analysis, interpretation, or preparation of this manuscript. All content was prepared, reviewed, and approved by the authors.

Nomenclature

B	Sisko fluid parameter
B_0	Magnetic field strength
Pr	Prandtl number
V_0	Suction parameter
M	Magnetic field
Q	Heat source
Fr	Darcy Forchheimer
R	Thermal radiation
U_w & V_w	Stretching velocities in x and y directions (m/s)
Cf	Skin friction
Nu	Nusselt number
qr	Radiative heat flux (W/m^2)
D_B	Brownian diffusivity (m^2/s)
C_b	Specific heat at constant pressure (J/kg. K)
T	Temperature (K)
C	Concentration (mol/m^3)
Sc	Schmidt number
f'&g'	Dimensionless velocities
k*	Mean absorption coefficient
Sh	Sherwood number
u, v, w	Components of velocity along x, y,z directions (m/s)
Kr	Chemical reaction

Greek words

λ&γ	Velocity slip parameters
β	Concentration slip parameter
ξ	Temperature slip parameter
ν	Kinematic viscosity (m^2/s)
σ*	Stefan-Boltzmann constant
σ	Electrical conductivity (S/m)
ρ	Density
μ	Dynamic viscosity (Kg/ms)
θ&ϕ	Dimensionless temperature and concentration
η	Similarity variable

References

[1] Bisht and R. Sharma, “Numerical Investigation of Sisko Nanofluid Over a Nonlinear Stretching Sheet with Convective Boundary Conditions,” Int J Multiscale Comput Eng, vol. 19, no. 1, pp. 41–54, 2021, doi: 10.1615/IntJMultCompEng.2021029649.

[2] Islam, M. Ferdows, MD. Shamshuddin, M. S. Alqarni, and Usman, “Sisko fluid modeling and numerical convective heat transport analysis over-stretching device with radiation and heat dissipation,” Numeri Heat Transf a Appl, vol. 85, no. 8, pp. 1240–1258, Apr. 2024, doi: 10.1080/10407782.2023.2200046.

[3] Kumar C, A. J. Benazir, and C. S. Ramesh, “Numerical investigation of heat and mass transfer of SWCNT/MWCNT-water suspension over a porous stretching sheet using Sisko fluid model,” ZAMM - Journal of Applied Mathematics and Mechanics / Zeitschrift für Angewandte Mathematik und Mechanik, vol. 104, no. 12, Dec. 2024, doi: 10.1002/zamm.202300573.

[4] Sohail, S. T. Abbas, and K. Abodayeh, "Investigation of mass and heat transport in bi-directional stretched flow of Sisko fluid with variable magnetic field and radiation effects via OHAM," Advances in Mechanical Engineering, vol. 16, no. 11, Nov. 2024, doi: 10.1177/16878132241288093.

[5] Adilakshmi, A. Akgül, G. Venkata Ramana Reddy, and M. Khan Hassani, "Thermal radiation and diffusion effects on MHD sisko fluid flow over a nonlinearly stretchable porous sheet," Boundary Value Problems, vol. 2025, no. 1, p. 97, Jul. 2025, doi: 10.1186/s13661-025-02042-6.

[6] Bhuiyan, MD. Shamshuddin, Usman, T. Islam, and M. Ferdows, "A numerical simulation of electrically conducting Sisko fluid flow with melting heat transfer, nonlinear convection and variable thermal conductivity constraints over an inclined electromagnetic sheet," ZAMM - Journal of Applied Mathematics and Mechanics / Zeitschrift für Angewandte Mathematik und Mechanik, vol. 105, no. 2, Feb. 2025, doi: 10.1002/zamm.202200464.

[7] Bhanu Lakshmi, K. Gangadhar, and K. Dasaradha Ramaiah, "Optimization of chemical and radiation reaction effects on magnetized bioconvective flow in 3D Sisko fluid with gyrotactic microorganisms using surface response methodology," Int J Mod Phys B, vol. 39, no. 23, Sep. 2025, doi: 10.1142/S0217979225502182.

[8] Abbas, H. Alotaibi, T. Muhammad, J. F. Gómez-Aguilar, A. A. Faqihi, H. A. Jari and A. A. Altherwi, "Significance of Marangoni convection and heat generation on Darcy Forchheimer 3D flow of Maxwell AA7072+AA7075-CH_3OHhybrid nanofluid over a rotating disk," J Therm Anal Calorim, vol. 150, no. 3, pp. 1967–1981, Feb. 2025, doi: 10.1007/s10973-024-13778-1.

[9] Shanmugapriya, S. Raman, and Abdu Alameri, "Heat Transport Efficiency of Magnetized AA7072/H_2 O Nanofluid and AA7072 + AA7075/ H_2O Hybrid Nanofluid Past a Non-Linear Porous Stretching Sheet," Biointerface Res Appl Chem, vol. 14, no. 1, p. 24, Feb. 2024, doi: 10.33263/BRIAC141.024.

[10] Patgiri and A. Paul, "Heat and Mass Transportation Enhancement of Casson Cu-AA7075-AA7072/Methanol Tri-Hybrid Nanofluid Flow Past a Porous Spinning Disk," in Heat Transfer Enhancement Techniques, Wiley, 2025, pp. 311–330. doi: 10.1002/9781394270996.ch14.

[11] Farooq, U. Farooq, H. Liu, A. Basem, N. Fatima, A. Alhushaybari, M. Imran, N. B. Ali, and T. Muhammad "Computational investigation of methanol-based hybrid nanofluid flow over a stretching cylinder with Cattaneo–Christov heat flux," J Comput Des Eng, vol. 11, no. 4, pp. 73–82, Jul. 2024, doi: 10.1093/jcde/qwae059.

[12] Chafai, H. Salhi, K. Benobouguerra, and S. Chafaa, "Numerical Study of Natural Convection of Nanofluids in an Inclined Flat Bottom Flask Using Finite-Volume Approach," Iran. J. Chem. Chem. Eng, vol. 41, no. 7, pp. 2454–2467, 2022.

[13] Salhi and N. Chafai, "Evaluation of the Thermal Conductivity of Nanofluids Using Statistical Analysis Methods," Nanoscience and Technology: An International Journal, vol. 13, no. 4, pp. 45–61, 2022, doi: 10.1615/NanoSciTechnolIntJ.2022043360.

[14] Baiti, H. Salhi, and N. Chafai, "Numerical investigation of turbulent mixed convection in a round bottom flask using a hybrid nanofluid," Advances in Mechanical Engineering, vol. 15, no. 9, Sep. 2023, doi: 10.1177/16878132231195022.

[15] Salhi and N. Chafai, "Numerical Simulation of Heat Transfer in a Square Cavity Filled with Hybrid Nanofluid," Nanoscience and Technology: An International Journal, vol. 15, no. 2, pp. 79–94, 2024, doi: 10.1615/NanoSciTechnolIntJ.2023049212.

[16] Salhi, N. Chafai, I. Moussaoui, and A. Mahamdi, "Influence of Hybrid Nanofluids and Source Configuration on Natural Convection in Square Cavity," Nanoscience and Technology: An International Journal, vol. 15, no. 4, pp. 65–78, 2024, doi: 10.1615/NanoSciTechnolIntJ.2024050935.

[17] Salhi, M. Si-Ameur, and D. Haddad, "Numerical Study of Natural Convection Heat Transfer Performance in An Inclined Cavity with Complex-Wavy-Wall: Nanofluid and Random Temperature," Computational Thermal Sciences: An International Journal, vol. 7, no. 1, pp. 51–64, 2015, doi: 10.1615/ComputThermalScien.2015013084.

[18] Salhi, N. Chafai, K. Benbouguerra, K. K. Yadav, M. Khalid, and G. S. Albakri, "Correlation between thermal conductivity of nanofluids and their structural, electronic and thermodynamic properties: DFT study," Inorganica Chim. Acta, vol. 589, p. 122919, Jan. 2026, doi: 10.1016/j.ica.2025.122919.

[19] H. Khan, W. A. Khan, S. M. Ibrahim, K. Swain, and Z. Huang, "Impact of multiple slips and thermal radiation on heat and mass transfer in MHD Maxwell hybrid nanofluid flow over porous stretching sheet," Case Studies in Thermal Engineering, vol. 61, p. 104906, Sep. 2024, doi: 10.1016/j.csite.2024.104906.

[20] Padmavathi, S. G. Kumar, G. Charankumar, S.V.K. Varma, E. Gouthami, G. Jayalalitha, B. M. M. Rao, V. Govindan, B. Pimpunchat, and H. Byeon, "Numerical study on thermal radiation and chemical reaction impacts on Prandtl nanofluid flow over a bilinear stretching sheet with heat generation and absorption: Response surface methodology," Nano-Structures & Nano-Objects, vol. 41, p. 101446, Feb. 2025, doi: 10.1016/j.nanoso.2025.101446.

[21] Padmavathi, V. Sannu, P. K. D. N. Murthy, V. V. Sibyala, G. Charankumar, M. A. Qureshi, K. Guedri, S. M. Hussain, A. H. Almaliki, M. Bayra., "Optimization of 3D hydromagnetic Casson fluid flow over a permeable stretching surface using RSM and AI," J Radiat Res Appl Sci, vol. 18, no. 2, p. 101554, Jun. 2025, doi: 10.1016/j.jrras.2025.101554.

[22] H. Elhag, "Numerical Study on 3D MHD Darcy-Forchheimer Flow Caused by Gyrotactic Microorganisms of the Bio-Convective Casson Nanofluid across a Stretched Sheet," Frontiers in Heat and Mass Transfer, vol. 22, no. 1, pp. 377–395, 2024, doi: 10.32604/fhmt.2023.044428.

[23] Zhang, R. R. Vaddemani, A. Ganjikunta, S. Bingi, and R. Kodi, “3D-MHD mixed convection in a darcy-forchheimer maxwell fluid: Thermo diffusion, diffusion-thermo effects, and activation energy influence,” Case Studies in Thermal Engineering, vol. 61, p. 104916, Sep. 2024, doi: 10.1016/j.csite.2024.104916.

[24] Manjunatha, J. S. Kumar, and S. V. K. Varma, “Impacts of heat generation and Buoyancy forces on hyperbolic Tangent Magneto ferrofluid flow with Darcy–Forchheimer model over a nonlinear stretching sheet: RSM analysis,” The European Physical Journal Plus, vol. 140, no. 6, p. 577, Jun. 2025, doi: 10.1140/epjp/s13360-025-06477-9.

[25] Nirisha, S. Sreedhar, V. Nagaradhika, S. Manjunatha, S. Ramesh, and O. Anwar Beg, “Modeling Joule heating in magnetized porous structures using statistical techniques,” Mech Time Depend Mater, vol. 29, no. 2, p. 53, Jun. 2025, doi: 10.1007/s11043-025-09793-w.

[26] Manjunatha, J. S. Kumar, K. U. Rehman, W. Shatanawi, and S. V. K. Varma, “Thermal radiation and thermo-diffusion in Casson-ferrofluid over a magnetized porous surface: RSM analysis,” International Journal of Thermofluids, vol. 26, p. 101130, Mar. 2025, doi: 10.1016/j.ijft.2025.101130.

[27] M and P. De, “Comparative study of hybrid, trihybrid and tetra-hybrid nanoparticles in MHD unsteady flow with chemical reaction, activation energy, Soret-Dufour effect and sensitivity analysis over Non-Darcy porous stretching cylinder,” Heliyon, vol. 10, no. 15, p. e35731, Aug. 2024, doi: 10.1016/j.heliyon. 2024.e35731.

[28] Nasir and A. S. Berrouk, “Numerical investigation of chemical reactive MHD fluid dynamics over a porous surface with Cattaneo–Christov heat flux,” J Therm Anal Calorim, vol. 149, no. 24, pp. 14877–14900, Dec. 2024, doi: 10.1007/s10973-024-13815-z.

[29] V. Krishna, “Hall and ion slip effects on the MHD flow of Casson hybrid nanofluid past an infinite exponentially accelerated vertical porous surface,” Waves in Random and Complex Media, vol. 34, no. 5, pp. 4658–4687, Sep. 2024, doi: 10.1080/17455030.2021.1998727.

[30] V. Krishna and K. Vajravelu, “Hall effects on the unsteady MHD flow of the Rivlin–Ericksen fluid past an infinite vertical porous plate,” Waves in Random and Complex Media, vol. 35, no. 4, pp. 7014–7037, Jul. 2025, doi: 10.1080/17455030.2022.2084178.

[31] R. Eid, A. Alsaedi, T. Muhammad, and T. Hayat, “Comprehensive analysis of heat transfer of gold-blood nanofluid (Sisko-model) with thermal radiation,” Results Phys, vol. 7, pp. 4388–4393, 2017, doi: 10.1016/j.rinp.2017.11.004.

[32] Waqas, U. Farooq, T. Muhammad, and U. Manzoor, “Importance of shape factor in Sisko nanofluid flow considering gold nanoparticles,” Alexandria Engineering Journal, vol. 61, no. 5, pp. 3665–3672, May 2022, doi: 10.1016/j.aej.2021.09.010.

[33] Jyothi, A. Dasore, R. Ganapati, Sk. M. Shareef, A. J. Chamkha, and V. R. Prasad, “Comparative Numerical Analysis of Heat and Mass Transfer Characteristics in Sisko Al2O3-Eg and TiO2-Eg Fluids on a Stretched Surface,” Frontiers in Heat and Mass Transfer, vol. 22, no. 1, pp. 79–105, 2024, doi: 10.32604/fhmt.2024.046891.

[34] N. Tanuja, L Kavitha, S. V. K. Varma, V. C. C. Raju, G. C. Kumar, M. R. Eid, and S. M. Hussain, “Heat and mass transfer analysis of Casson-based hybrid nanofluid flow in the presence of an aligned magnetic field: An application toward mechanical engineering,” Proceedings of the Institution of Mechanical Engineers, Part N: Journal of Nanomaterials, Nanoengineering and Nano systems, May 2024, doi: 10.1177/23977914241248546.

[35] Tlili, H. A. Nabwey, G. P. Ashwinkumar and N. Sandeep, “3-D magnetohydrodynamic AA7072-AA7075/methanol hybrid nanofluid flow above an uneven thickness surface with slip effect,” Scientific Reports, 10, 4265, 2020, doi: https://doi.org/10.1038/s41598-020-61215-8

[36] Manjunatha, J. Santhosh Kumar, M. Veera Krishna, S. V. K. Varma, ANN modelling on heat and mass transfer in MHD chemically reactive and radiative flow of hybrid ferrofluid over a non-linear stretching porous surface. Multiscale and Multidisciplinary Modeling, Experiments and Design, vol. 8, no. 6, 2025, https://doi.org/10.1007/s41939-025-00879-z.

[37] N.Tanuja, L. Kavitha, K. U. Rehman, S.V.K Varma, W. Shatanawi, G. V. Kumar “Parametric analysis for thermally magnetized hybrid ternary(TMHT)nanofluid flow on thin film with temperature stratification,” International Journal of Thermofluids, vol. 26, p. 101089, Mar. 2025, doi: 10.1016/j.ijft.2025.101089.

[38] Manjunatha, B. Ammani Kuttan, and T. N. Tanuja, “Sensitivity analysis of thermal optimisation within conical gap between the cone and the surface of disk with particle deposition,” J Therm Anal Calorim, vol. 150, no. 1, pp. 361–375, Jan. 2025, doi: 10.1007/s10973-024-13866-2.

[39] B. Pavithra, R. Sharma, V. Nagaradhika, and S. Manjunatha, “Statistical Study of Hybrid Nanofluid Heat Transfer in Porous Rotating Cone,” Journal of Mines, Metals and Fuels, pp. 3523–3541, Nov. 2025, doi: 10.18311/jmmf/2025/49720.